Data-driven refinement of an analytical holographic model for the QCD phase transition

Xun Chen,[1,2,*] Floriana Giannuzzi,[2,†] and Stefano Nicotri[2,‡]

[1]*School of Nuclear Science and Technology, University of South China, Hengyang 421001, China*
[2]*INFN—Istituto Nazionale di Fisica Nucleare—Sezione di Bari Via Orabona 4, 70125 Bari, Italy*

(Received 5 December 2025; accepted 8 April 2026; published 8 May 2026)

Using $(2+1)$-flavor lattice QCD data, we refine the parameters of an analytical holographic model via gradient descent optimization to precisely locate the critical endpoint in the T-μ plane. Specifically, we calibrate the model using input data for the speed of sound at $\mu_B = 0$, the second-order baryon number susceptibility χ_2^B, and the baryon number density at $\mu_B/T = 1$. With these parameters fixed, we calculate pressure and energy density versus temperature at small chemical potentials and compare the results with lattice QCD data using Taylor expansion techniques. This comparison validates the robustness of our model upon extension to finite chemical potentials, as the results show broad consistency with lattice QCD data in this regime. Finally, we employ the calibrated model to determine the coordinates of the critical endpoint in the T-μ_B plane, finding it located at $(\mu_B = 0.678\ \text{GeV}, T = 0.110\ \text{GeV})$.

DOI: 10.1103/j7wh-vf6x

I. INTRODUCTION

The phase structure of strongly interacting matter described by QCD at finite temperature and baryon chemical potential is of fundamental importance in high-energy nuclear physics. First-principles lattice QCD simulations have successfully established that, at vanishing chemical potential, the transition from hadronic matter to the quark-gluon plasma (QGP) is a smooth crossover for physical quark masses [1–3]. However, the sign problem prevents direct Monte Carlo calculations at finite baryon density, leaving the possible existence and location of a critical endpoint (CEP)—where the crossover turns into a first-order phase transition—an open question of significant theoretical and experimental interest [4,5]. A recent review of CEP can be found in Ref. [6].

Various approaches have been developed to explore the QCD phase diagram beyond the lattice-accessible region, including functional renormalization group methods (FRG) [7–10], Dyson-Schwinger equations (DSE) [11–13], and effective models like the Polyakov-loop-extended Nambu-Jona-Lasinio (PNJL) model [14–16]. Among these, holographic QCD models, based on the gauge/gravity duality, offer a compelling nonperturbative framework that remains applicable at strong coupling and finite density [17–24]. In particular, Einstein-Maxwell-Dilaton (EMD) models have been used to successfully capture QCD thermodynamics, transport, and phase structure by incorporating dilaton and gauge field dynamics in a five-dimensional gravitational theory [25–53].

In this work, we develop a data-driven analytical EMD holographic model by calibrating its parameters against state-of-the-art $(2+1)$-flavor lattice QCD data at zero and finite baryon chemical potential. Employing a gradient descent optimization scheme, we constrain the metric warp factor and gauge kinetic function to reproduce lattice observables such as the speed of sound, baryon number susceptibility, and baryon density. In particular, at odds with previous studies, we fix parameters using also data at small values of chemical potential. We then extend the model to predict the QCD equation of state and locate the CEP in the T-μ plane. Our results show quantitative agreement with lattice calculations and other holographic predictions, reinforcing the model's reliability in exploring the inaccessible regions of the QCD phase diagram.

II. REVIEW OF EMD FRAMEWORK

We begin by reviewing the five-dimensional Einstein-Maxwell-Dilaton system. The action describes a gravitational field $g_{\mu\nu}$, a Maxwell field A_μ and a dilaton field ϕ. Since we are only interested in the time component $A_0(z) = A_t(z)$, we set $A_i = 0$ and make a gauge choice $A_z = 0$. In the Einstein frame, the action is given by

*Contact author: chenxun@usc.edu.cn
†Contact author: floriana.giannuzzi@ba.infn.it
‡Contact author: nicotri@infn.it

Published by the American Physical Society under the terms of the Creative Commons Attribution 4.0 International license. Further distribution of this work must maintain attribution to the author(s) and the published article's title, journal citation, and DOI. Funded by SCOAP³.

$$S_b = \frac{1}{16\pi G_5}\int d^5x\sqrt{-g}\Big[R - \frac{f(\phi)}{4}F^2 - \frac{1}{2}\partial_\mu\phi\partial^\mu\phi - V(\phi)\Big], \tag{1}$$

where $f(\phi)$ is the gauge kinetic function describing the coupling between the dilaton ϕ and the Maxwell field A_μ (whose strength is F^2), $V(\phi)$ is the potential of the dilaton field, and G_5 is the Newton constant in five dimensions. We use the metric ansatz,

$$ds^2 = \frac{L^2e^{2A(z)}}{z^2}\left[-g(z)dt^2 + \frac{dz^2}{g(z)} + d\vec{x}^2\right], \tag{2}$$

where z is the fifth-dimensional holographic coordinate and the radius L of AdS_5 space is set to unity. Using the metric ansatz, the equations of motion and constraints for the background fields are

$$\phi'' + \phi'\left(-\frac{3}{z} + \frac{g'}{g} + 3A'\right) - \frac{L^2e^{2A}}{z^2g}\frac{\partial V}{\partial\phi} + \frac{z^2e^{-2A}A_t'^2}{2L^2g}\frac{\partial f}{\partial\phi} = 0, \tag{3}$$

$$A_t'' + A_t'\left(-\frac{1}{z} + \frac{1}{f}\frac{\mathrm{d}f}{\mathrm{d}z} + A'\right) = 0, \tag{4}$$

$$g'' + g'\left(-\frac{3}{z} + 3A'\right) - \frac{e^{-2A}A_t'^2z^2f}{L^2} = 0, \tag{5}$$

$$A'' + \frac{g''}{6g} + A'\left(-\frac{6}{z} + \frac{3g'}{2g}\right) - \frac{1}{z}\left(-\frac{4}{z} + \frac{3g'}{2g}\right) + 3A'^2 + \frac{L^2e^{2A}V}{3z^2g} = 0, \tag{6}$$

$$A'' - A'\left(-\frac{2}{z} + A'\right) + \frac{\phi'^2}{6} = 0. \tag{7}$$

Only four of the above five equations are independent. The boundary conditions at the horizon are

$$A_t(z_h) = g(z_h) = 0. \tag{8}$$

Near the asymptotic boundary $z \to 0$, we require the metric in the string frame to be asymptotic to AdS_5. The boundary conditions at $z = 0$ are

$$A(0) = -\sqrt{\frac{1}{6}}\phi(0), \qquad g(0) = 1, \tag{9}$$

and the boundary behavior of the Maxwell field is

$$A_t(z \to 0) = \mu + \rho' z^2 + \cdots, \tag{10}$$

where μ denotes the baryon chemical potential, related to the quark chemical potential by $\mu = \mu_B = 3\mu_q$ and ρ' is a coefficient proportional to the baryon number density. The density itself is calculated as [25,54]

$$\rho = \left|\lim_{z\to 0}\frac{\partial\mathcal{L}}{\partial(\partial_z A_t)}\right| = -\frac{1}{16\pi G_5}\lim_{z\to 0}\left[\frac{\mathrm{e}^{A(z)}}{z}f(\phi(z))A_t'(z)\right], \tag{11}$$

where $\mathcal{L}$ is the Lagrangian density in the Einstein frame. The equations of motion admit the following analytical expressions:

$$\begin{aligned}
\phi'(z) &= \sqrt{-6\left(A'' - A'^2 + \frac{2}{z}A'\right)},\\
A_t(z) &= \sqrt{\frac{-1}{\int_0^{z_h} y^3e^{-3A}dy\int_{y_g}^{y}\frac{x}{e^Af}dx}}\int_z^{z_h}\frac{y}{e^Af}dy,\\
g(z) &= 1 - \frac{\int_0^z y^3e^{-3A}(\int_{y_g}^{y}\frac{x}{e^Af}dx)dy}{\int_0^{z_h} y^3e^{-3A}(\int_{y_g}^{y}\frac{x}{e^Af}dx)dy},\\
V(z) &= \frac{-3z^2ge^{-2A}}{L^2}\left[A'' + 3A'^2 + \frac{g''}{6g} + \left(\frac{3g'}{2g} - \frac{6}{z}\right)A' - \frac{1}{z}\left(\frac{3g'}{2g} - \frac{4}{z}\right)\right].
\end{aligned} \tag{12}$$

The integration constant y_g is related to the chemical potential μ by the boundary condition in (10), yielding,

$$\mu = \sqrt{\frac{-1}{\int_0^{z_h} y^3e^{-3A(y)}\left(\int_{y_g}^{y}\frac{x}{e^{A(x)}f(x)}dx\right)dy}}\int_0^{z_h}\frac{y}{e^{A(y)}f(y)}dy. \tag{13}$$

We adopt a general ansatz for the gauge kinetic function,

$$f(z) = \frac{ke^{cz^2+hz^4+nz^6-A(z)}}{-2c - 4hz^2 - 6nz^4}. \tag{14}$$

In this case, Eq. (13) simplifies and the relation between the integration constant y_g and the chemical potential μ becomes

$$e^{-cy_g^2-hy_g^4-ny_g^6} = \frac{I_2(0,z_h)}{I_1(0,z_h)} + \frac{(e^{-cz_h^2-hz_h^4-nz_h^6}-1)^2}{k\mu^2I_1(0,z_h)}, \tag{15}$$

where

$$I_1(a,b) = \int_a^b y^3 e^{-3A(y)}\, dy,$$
$$I_2(a,b) = \int_a^b y^3 e^{-3A(y)-cy^2-hy^4-ny^6}\, dy. \tag{16}$$

Consequently, the solutions can be written in the following simplified forms:

$$\begin{aligned}
g(z) &= 1 - \frac{1}{I_1(0,z_h)}\left[I_1(0,z) - \frac{\mu^2 k}{\Delta^2}\det \mathcal{G}\right],\\
\phi'(z) &= \sqrt{6(A'^2 - A'' - 2A'/z)},\\
A_t(z) &= \mu \frac{e^{-cz^2-hz^4-nz^6} - e^{-cz_h^2-hz_h^4-nz_h^6}}{1 - e^{-cz_h^2-hz_h^4-nz_h^6}},\\
V(z) &= \frac{-3z^2 g e^{-2A}}{L^2}\left[A'' + 3A'^2 + \frac{g''}{6g}\right.\\
&\quad \left. + \left(\frac{3g'}{2g} - \frac{6}{z}\right)A' - \frac{1}{z}\left(\frac{3g'}{2g} - \frac{4}{z}\right)\right],
\end{aligned} \tag{17}$$

with

$$\Delta = e^{-cz_h^2-hz_h^4-nz_h^6} - 1, \tag{18}$$

and

$$\det \mathcal{G} = \begin{vmatrix} I_1(0,z_h) & I_2(0,z_h) \\ I_1(z_h,z) & I_2(z_h,z) \end{vmatrix}. \tag{19}$$

The Hawking temperature and entropy of this black hole solution are given by

$$T = \frac{z_h^3 e^{-3A(z_h)}}{4\pi I_1(0,z_h)}\left[1 - \frac{\mu^2 k}{\Delta^2}((\Delta+1)I_1(0,z_h) - I_2(0,z_h))\right] \tag{20}$$

and

$$s = \frac{e^{3A(z_h)}}{4G_5 z_h^3}. \tag{21}$$

To obtain an analytical solution, we assume the form

$$A(z) = d * \ln(az^2+1) + d * \ln(bz^4+1). \tag{22}$$

The corresponding metric function in the string frame is $A_s(z) = A(z) + \sqrt{\frac{1}{6}}\phi(z)$. The first four parameters (a, b, d, G_5) will be fixed by matching the equation of state obtained in the holographic model with lattice QCD data using a gradient-based parameter optimization, as described in the next section. The other parameters (c, k, h, and n) will be constrained by the baryon number susceptibility and baryon number density. Once the entropy and the density ρ are determined, other thermodynamic functions can be computed. The specific heat at constant volume is given by [17]

$$C_V = T\frac{\partial s}{\partial T}. \tag{23}$$

At nonzero chemical potential, the squared speed of sound can be calculated by [26,27,55]

$$C_s^2 = \frac{s}{T\left(\frac{\partial s}{\partial T}\right)_\mu + \mu\left(\frac{\partial \rho}{\partial T}\right)_\mu}, \tag{24}$$

and the second-order baryon number susceptibility is defined as

$$\chi_2^B = \frac{1}{T^2}\frac{\partial \rho}{\partial \mu}. \tag{25}$$

The free energy and pressure are calculated integrating the thermodynamic relation,

$$dF = -dp = -sdT - \rho d\mu, \tag{26}$$

as in [25,41]. We have normalized the free energy to vanish at $(T,\mu) = (0,0)$. Then, the energy density of the system can be derived as

$$\epsilon = -p + sT + \mu\rho. \tag{27}$$

In this EMD model, based on potential reconstruction method, the warp factor $A(z)$ is fixed as input while the dilaton potential is obtained from the equations of motion as a function of z. The resulting $V(\phi)$ exhibits a slight dependence on the phase space, so it does not retain the same functional form for different values of z_h and μ_B, whereas the dilaton itself is independent of temperature and chemical potential. As a consequence, if the pressure is calculated from Eq. (26) using the entropy and density derived from (21) and (11), respectively, the result does not yield an exact differential, leading to inconsistent Maxwell relations. Nevertheless, as shown in the Appendix, although the computed pressure may yield different values depending on the chosen integration path, the resulting discrepancies in the values we find for pressure and energy density turn out to be very small. In the Appendix we have also numerically shown that the potential $V(\phi)$ is almost independent on z_h and μ_B, since curves of V versus ϕ obtained at different temperatures and chemical potentials almost overlap except in a small region close to the black-hole horizon, where small differences are observed. A similar check has been proposed in [56–58].

TABLE I. Optimized model parameters from lattice QCD calibration.

Parameter	Value	Parameter	Value
a	0.2219 GeV^2	k	0.02243 GeV^2
b	0.0330 GeV^4	n	−0.0010 GeV^6
c	−0.0358 GeV^2	h	0.0039 GeV^4
d	−0.1212	G_5/L^3	0.4113

III. THERMODYNAMICS AND PHASE DIAGRAM

The model is calibrated through an iterative process against the lattice results. Specifically, we use a gradient descent optimizer to automatically adjust the model parameters, thereby minimizing the difference between the holographic outcomes and lattice calculations. Further details can be found in Refs. [39,41]. We calibrated our model using lattice QCD data for the following observables; the speed of sound at $\mu_B = 0$, the second-order baryon number susceptibility χ_2^B, and the baryon number density at $\mu_B/T = 1$ [59–61]. The values of the parameters obtained from this calibration are shown in Table I.

The thermodynamic behavior of the system at vanishing baryon chemical potential is summarized in Fig. 1. Panel (a) displays the temperature dependence of key thermodynamic quantities; entropy density s, energy density ϵ, pressure p, and the trace anomaly $\epsilon - 3p$, all normalized by a proper power of T, according to their scaling at large temperature. The predictions of the holographic model (solid red curves) show remarkable agreement with lattice QCD data across the entire temperature range. Particularly noteworthy is the model's ability to capture the rapid rise of these quantities during the crossover transition from the confined to the deconfined phase. The trace anomaly, which serves as a sensitive indicator of the transition region, exhibits a characteristic peak that is well-reproduced by the holographic approach. This agreement demonstrates that our model correctly captures the nonperturbative dynamics near the transition temperature T_c. At high temperatures ($T \gtrsim 2T_c$), all quantities approach their respective Stefan-Boltzmann limits [62], as expected for a weakly interacting quark-gluon plasma. The holographic model smoothly interpolates between the strongly coupled regime near T_c and the weakly coupled limit at high temperatures, providing a unified description of the equation of state. Panel (b) of Fig. 1 shows the second-order baryon number susceptibility χ_2^B, which measures the response of the baryon density to changes in the chemical potential and serves as a probe of the relevant degrees of freedom in the system. The comparison includes lattice QCD data with different temporal extents N_τ (various symbols) as well as continuum extrapolated results (gray squares).

Figure 2(a) displays the temperature dependence of the baryon number density ρ/T^3 at finite chemical potential μ_B, with results shown for several representative values of μ_B/T. Figure 2(b) displays the temperature dependence of second-order baryon number susceptibility χ_2^B for two representative values of μ_B/T. The predictions of the holographic model (HQCD, red dashed curves) are compared with lattice QCD results obtained from $[n, 4]$ Padé approximants (gray bands) and conventional Taylor expansions truncated at $O((\mu_B/T)^7)$ (blue bands) [63]. The HQCD model successfully captures the characteristic increase in baryon density with increasing chemical potential across the entire temperature range.

Figure 3(a) shows the temperature dependence of the squared speed of sound C_s^2 at $\mu_B = 0$, which provides crucial information about the conformal behavior and stiffness of the equation of state. The holographic model (solid black curve) exhibits a smooth, monotonic increase from $C_s^2 \approx 0.15$ at $T = 150$ MeV to approximately 0.30 at $T = 400$ MeV, indicating a gradual approach toward the conformal limit of $C_s^2 = 1/3$ [62]. The excellent agreement between the HQCD predictions and lattice QCD data

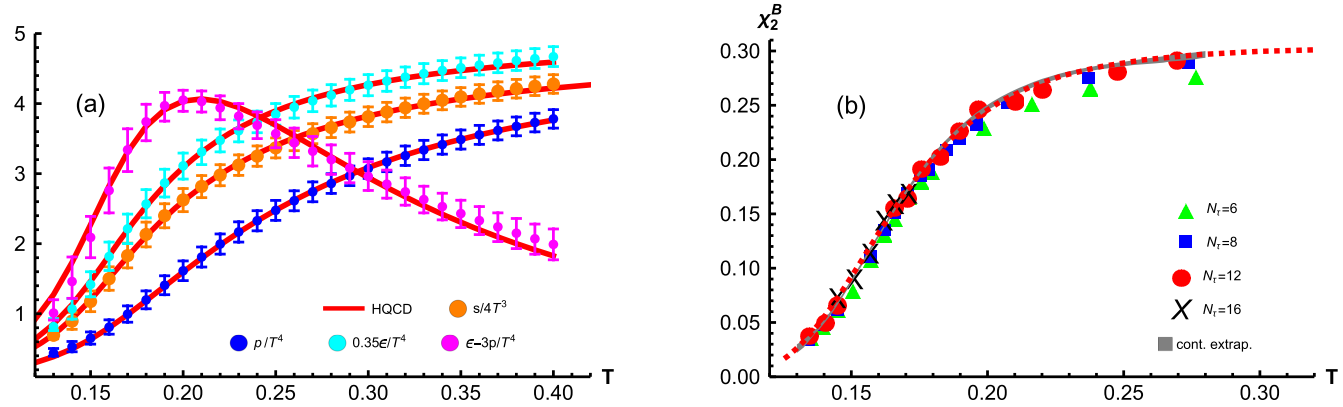


FIG. 1. Comparison of $(2+1)$-flavor lattice QCD [59–61] and holographic model predictions for (a) thermodynamic quantities (entropy s, energy ϵ, pressure p, trace anomaly $\epsilon - 3p$) versus temperature at vanishing chemical potential, (b) second-order baryon number susceptibility versus temperature at vanishing chemical potential.

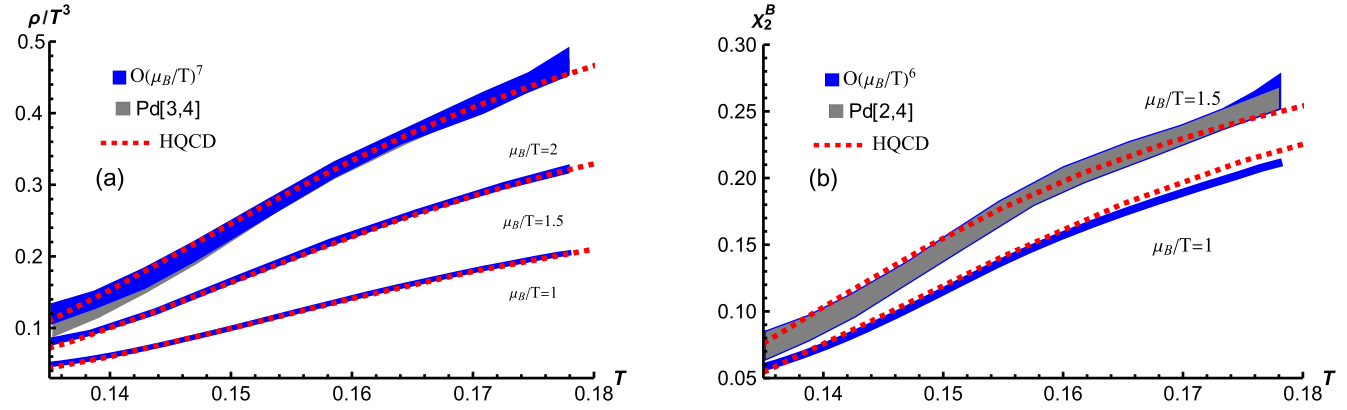


FIG. 2. Comparison of $(2+1)$-flavor lattice QCD [63] and holographic model predictions for (a) baryon number density versus temperature at finite chemical potential, (b) second-order baryon number susceptibility versus temperature at finite chemical potential.

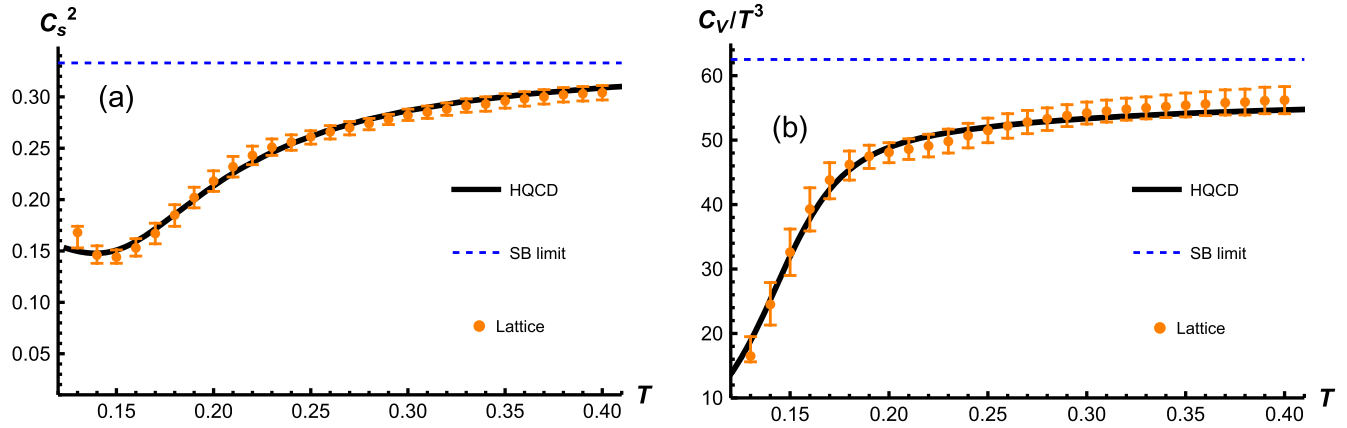


FIG. 3. Comparison between $(2+1)$-flavor lattice QCD [59] and holographic model predictions at zero chemical potential for (a) temperature dependence of the squared speed of sound, (b) temperature dependence of the specific heat.

(orange points) demonstrates that the model correctly captures the restoration of conformal symmetry at high temperatures. The smooth progression without any discontinuities is consistent with the crossover nature of the QCD transition at physical quark masses. Particularly noteworthy is the model's ability to reproduce the low-temperature behavior where C_s^2 exhibits a minimum near the transition region, reflecting the softest point in the equation of state. The specific heat C_V/T^3, shown in Fig. 3(b), serves as a sensitive probe of thermodynamic fluctuations and degrees of freedom in the system. The comparison with lattice QCD data reveals generally good agreement, particularly in the high-temperature regime where the Stefan-Boltzmann limit $C_V/T^3 \approx 62.5$ [62] is gradually approached.

Figure 4(a) displays the temperature dependence of the normalized pressure p/T^4 at finite chemical potential. Pressure has been computed integrating Eq. (26) along the path $(0,0) \to (0,T) \to (\mu_B, T)$, in the same way in which lattice data have been obtained. More details are found in the Appendix. The holographic model shows good agreement with lattice QCD data across all values of μ_B/T investigated. The pressure exhibits a characteristic rapid increase in the transition region. A key observation is the enhancement of p/T^4 with increasing chemical potential μ_B/T, particularly noticeable in the intermediate temperature range. This enhancement reflects the additional contribution from finite baryon density to the equation of state. The holographic model successfully captures this dependence, demonstrating its capability to describe the thermodynamic properties of dense QCD matter. The smooth behavior of the pressure without any discontinuities is consistent with the crossover nature of the QCD transition at physical quark masses and at such small values of chemical potential.

The normalized energy density ϵ/T^4, shown in Fig. 4(b), provides complementary information about the equation of state. As in the case of the pressure, the holographic model predictions agree with lattice QCD results (some discrepancies are found at low T). The holographic model correctly reproduces the enhancement of ϵ/T^4 with increasing μ_B/T.

Figure 5(a) presents the QCD phase diagram in the temperature-chemical potential (T-μ) plane as predicted by

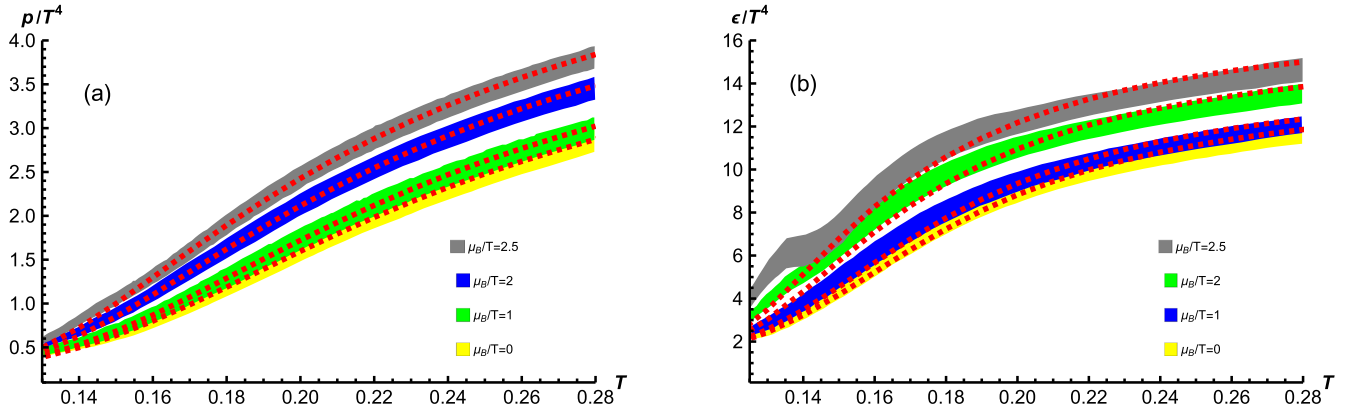


FIG. 4. (a) Comparison of pressure between our holographic model and lattice QCD data at various μ/T values [61], (b) Comparison of energy density ϵ between model predictions and lattice results at various μ/T values [61].

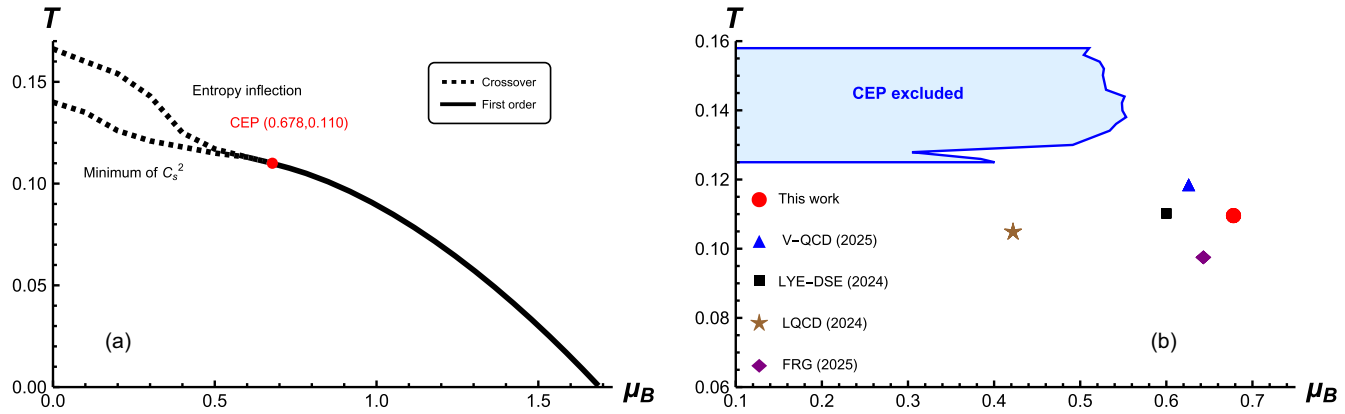


FIG. 5. (a) The QCD phase diagram in the T-μ plane, (b) Comparison of our model predictions with those of other theoretical models, including the CEP-excluded region from lattice QCD [66], the CEP position from lattice QCD ($\mu_B^{\mathrm{CEP}} = 422^{+80}_{-35}$ MeV, $T^{\mathrm{CEP}} = 105^{+8}_{-18}$ MeV) [67]; from V-QCD ($\mu_B^{\mathrm{CEP}} = 626^{+90}_{-179}$ MeV, $T^{\mathrm{CEP}} = 105^{+14}_{-6}$ MeV) [65]; from LYE-DSE [12], and from FRG [7].

this holographic model. The diagram clearly shows the characteristic features of the QCD phase structure; a crossover transition at small chemical potentials that evolves into a first-order phase transition at higher densities. We have chosen two definitions of the transition line in the crossover region, producing the two dashed lines shown in the figure. The upper line is obtained finding the inflection points of the s/T^3 versus T curves at fixed values of the chemical potential. The other line is obtained locating the minimum of the squared speed of sound as a function of temperature at fixed chemical potential. At values of the chemical potential higher than a critical one, the relation between temperature and z_h is no more a bijection and a first-order phase transition occurs [64]. In this case, a jump in some thermodynamic functions, as e.g., entropy and baryon number density, is found at the critical temperature, as shown in Fig. 6. The first-order transition line has been computed finding, for each value of the chemical potential, the temperature at which the free energy is the same in the two phases [17]. Analogously, we have found the same result with a different procedure, determining, at fixed chemical potential, the temperature T_f at which the closed regions bounded by the entropy density on either side of the $T = T_f$ line have equal area (for more details see [17]). The CEP, marked by the red circle at $(T_{\mathrm{CEP}}, \mu_{\mathrm{CEP}}) = (0.110, 0.678)$ GeV, represents the termination point of the first-order transition line. At this point, the phase transition becomes second order, with associated critical phenomena. The location of the CEP in our model falls within the theoretically expected range and is consistent with constraints from first-principles calculations. The smooth connection between the crossover and first-order transition regions demonstrates the model's ability to describe the entire phase structure consistently. As expected in chiral and deconfinement transitions, the transition temperature decreases as the chemical potential increases. Figure 5(b) provides a comparison of our model predictions with results from other theoretical approaches. This convergence suggests an emerging consensus within the

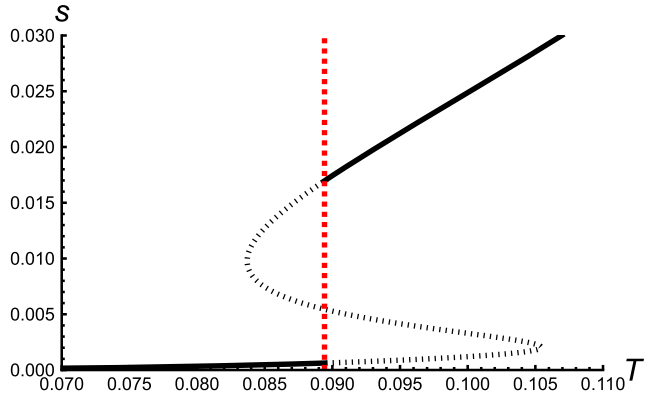


FIG. 6. Entropy density (in GeV^3) at $\mu = 1$ GeV as a function of temperature (in GeV). At $T \sim 89.4$ MeV a first-order phase transition occurs.

holographic frameworks regarding the location of the critical endpoint. Especially, the CEP position predicted by the holographic V-QCD model [65], whose parameters have been fixed from neutron star observations, is consistent with the result found in this model, constrained from lattice QCD. This agreement from two independent lines of evidence reinforces the validity of our model.

IV. CONCLUSION

In this work, we have established a refined analytical holographic model for QCD thermodynamics by systematically calibrating it against state-of-the-art $(2+1)$-flavor lattice QCD data with gradient-based parameter optimization. The model successfully describes the equation of state across a wide range of temperatures and baryon chemical potentials, demonstrating remarkable agreement with first-principles calculations. The improved agreement with lattice computations at zero and small chemical potential with respect to previous studies has been achieved by introducing two more parameters is the gauge kinetic function $f(\phi)$, and by calibrating the model using input data for the speed of sound at zero chemical potential, and also data at finite but small chemical potential concerning second-order baryon number susceptibility and baryon number density.

The core achievement of this study is the precise determination of the QCD phase diagram, as summarized in Fig. 5(a). Our model predicts a smooth crossover transition at low chemical potentials that evolves into a first-order phase transition at higher densities, culminating in a CEP located at $(\mu_{\mathrm{CEP}}, T_{\mathrm{CEP}}) = (0.678\ \mathrm{GeV}, 0.110\ \mathrm{GeV})$. This prediction is positioned within the broader landscape of theoretical approaches in Fig. 5(b), where it shows strong consistency with some recent results from other holographic QCD studies.

Beyond the phase structure, the model exhibits robust performance in reproducing fundamental and derived thermodynamic quantities. It accurately captures the behavior of the entropy density, pressure, energy density, and trace anomaly at $\mu_B = 0$, as well as the second-order baryon number susceptibility χ_2^B. Notably, at small chemical potential, our holographic predictions for the baryon number density show agreement with Padé-resummed lattice data and truncated Taylor expansions.

The comprehensive agreement between our holographic framework and lattice QCD data validates the use of such bottom-up models as a powerful and consistent tool for extrapolating into regions of the QCD phase diagram that are inaccessible to standard lattice simulations due to the sign problem. The successful description of the equation of state, along with the precise location of the CEP, provides valuable theoretical guidance for ongoing experimental searches in heavy-ion collision programs and contributes to a more profound understanding of dense matter in neutron stars.

ACKNOWLEDGMENTS

We thank P. Colangelo and F. De Fazio for fruitful discussions. This work is supported by the National Natural Science Foundation of China (NSFC) Grant No. 12405154, and the European Union—Next Generation EU through the research Grant No. P2022Z4P4B "SOPHYA—Sustainable Optimised PHYsics Algorithms: fundamental physics to build an advanced society" under the Program No. PRIN 2022 PNRR of the Italian Ministero dell'Università e Ricerca (MUR). This study has been carried out within the INFN project (Iniziativa Specifica) SPIF.

DATA AVAILABILITY

The data that support the findings of this article are openly available 7,12,59–61,63,65–67.

APPENDIX

In this model, the dilaton potential $V(\phi)$ is not given as input, but is computed as a function $V(z)$ from the equations of motion. In this case, the resulting potential $V(\phi)$ may get different functional forms when varying z_h and μ_B. In Fig. 7, $V(\phi)$ is plotted against the dilaton ϕ at some values of temperature and chemical potential, in particular in the region close to the CEP and at $\mu_B = 0$, where some lattice data are used to fit the parameters of the model. It can be observed that the curves almost overlap except in a small region close to the black-hole horizon.

Although differences among curves are small, they spoil the computation of pressure. As pointed out in the text, in EMD models based on potential reconstruction method the pressure defined in Eq. (26) may not be an exact differential, so it may get different values if integrated along different paths. For this reason, we have replicated Fig. 4(a) in Fig. 8 to show that differences coming from different integration paths are small. In Fig. 8, pressure has been computed from path $(0,0) \to (0,T) \to (\mu_B, T)$ (path 1) to

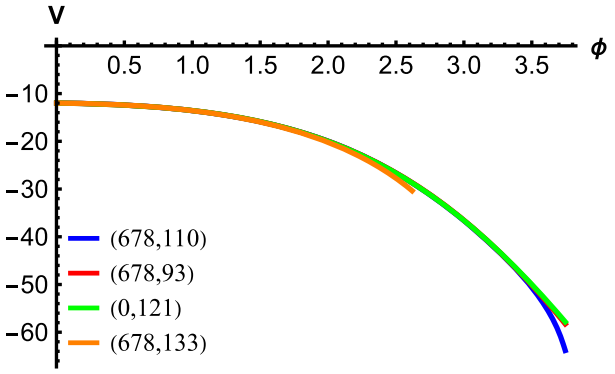


FIG. 7. Dilaton potential at the values of chemical potential and temperature (μ_B, T) (in MeV) indicated in the legend.

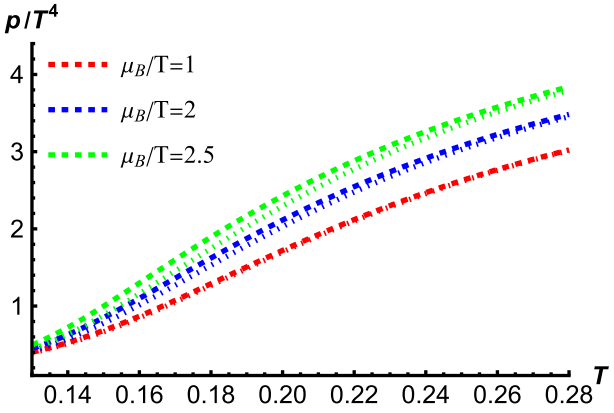


FIG. 8. Pressure as a function of temperature at fixed μ_B/T, indicated in the legend. Dashed curves have been obtained integrating Eq. (26) along path 1 $[(0,0) \to (0,T) \to (\mu_B, T)]$, dotted curves have been obtained integrating Eq. (26) along path 2 $[(0,0) \to (\mu_B, 0) \to (\mu_B, T)]$.

get the dashed curves, and from path $(0,0) \to (\mu_B, 0) \to (\mu_B, T)$ (path 2) to get dotted curves. Small deviations are found at higher chemical potential. We have used path 1 $[(0,0) \to (0,T) \to (\mu_B, T)]$ in Fig. 4, since the lattice points shown in the plot for comparison were obtained using such a path in Fig. 7 (left) of Ref. [61], i.e., taking results obtained by the HotQCD Collaboration [59] for pressure at finite temperature and zero chemical potential, and then adding the results from the $\mathcal{O}((\mu_B/T)^6)$ expansions presented in the paper.

[1] Y. Aoki, G. Endrodi, Z. Fodor, S. D. Katz, and K. K. Szabo, Nature (London) **443**, 675 (2006).
[2] A. Bazavov *et al.*, Phys. Rev. D **85**, 054503 (2012).
[3] S. Borsanyi, Z. Fodor, C. Hoelbling, S. D. Katz, S. Krieg, C. Ratti, and K. K. Szabo (Wuppertal-Budapest Collaboration), J. High Energy Phys. 09 (2010) 073.
[4] K. Fukushima and T. Hatsuda, Rep. Prog. Phys. **74**, 014001 (2011).
[5] M. A. Stephanov, Prog. Theor. Phys. Suppl. **153**, 139 (2004).
[6] M. Stephanov, EPJ Web Conf. **314**, 00042 (2024).
[7] W. J. Fu, X. Luo, J. M. Pawlowski, F. Rennecke, and S. Yin, Phys. Rev. D **111**, L031502 (2025).
[8] M. Osman, D. Hou, W. Wang, and H. Zhang, Eur. Phys. J. C **85**, 804 (2025).
[9] J. V. Roth, Y. Ye, S. Schlichting, and L. von Smekal, J. High Energy Phys. 01 (2025) 118.
[10] F. Murgana, V. Greco, M. Ruggieri, and D. Zappalà, Phys. Rev. D **109**, 096017 (2024).
[11] P. Isserstedt, M. Buballa, C. S. Fischer, and P. J. Gunkel, Phys. Rev. D **100**, 074011 (2019).
[12] Z.-Y. Wan, Y. Lu, F. Gao, and Y.-X. Liu, Eur. Phys. J. C **84**, 899 (2024).
[13] Y. Lu, F. Gao, Y.-X. Liu, and J. M. Pawlowski, Phys. Rev. D **110**, 014036 (2024).
[14] Z. Li, K. Xu, X. Wang, and M. Huang, Eur. Phys. J. C **79**, 245 (2019).
[15] L.-M. Liu, J. Xu, and G.-X. Peng, Nucl. Phys. Rev. **40**, 493 (2023).
[16] N. M. Bratovic, T. Hatsuda, and W. Weise, Phys. Lett. B **719**, 131 (2013).
[17] O. DeWolfe, S. S. Gubser, and C. Rosen, Phys. Rev. D **83**, 086005 (2011).
[18] U. Gursoy, E. Kiritsis, L. Mazzanti, and F. Nitti, Phys. Rev. Lett. **101**, 181601 (2008).
[19] C. Ecker, M. Järvinen, G. Nijs, and W. van der Schee, Phys. Rev. D **101**, 103006 (2020).
[20] Q. Fu, S. He, L. Li, and Z. Li, J. High Energy Phys. 06 (2025) 221.
[21] Y.-Q. Zhao, S. He, D. Hou, L. Li, and Z. Li, J. High Energy Phys. 04 (2023) 115.
[22] J. Grefa, J. Noronha, J. Noronha-Hostler, I. Portillo, C. Ratti, and R. Rougemont, Phys. Rev. D **104**, 034002 (2021).
[23] Z. Li, Phys. Rev. D **110**, 046012 (2024).
[24] Z.-R. Zhu, J.-X. Chen, X.-M. Liu, and D. Hou, Eur. Phys. J. C **82**, 560 (2022).
[25] R. Critelli, J. Noronha, J. Noronha-Hostler, I. Portillo, C. Ratti, and R. Rougemont, Phys. Rev. D **96**, 096026 (2017).
[26] Y. Yang and P.-H. Yuan, Phys. Rev. D **97**, 126009 (2018).
[27] M.-W. Li, Y. Yang, and P.-H. Yuan, J. High Energy Phys. 02 (2021) 055.
[28] Z. Li and F. Wang, arXiv:2507.09113.
[29] Z. Li, D. Li, and M. Huang, Phys. Rev. D **111**, 126019 (2025).

[30] X. Cao and H. Liu, Phys. Rev. D **111**, 026008 (2025).
[31] I. Y. Aref'eva, A. Hajilou, A. Nikolaev, and P. Slepov, Phys. Rev. D **112**, 126007 (2025).
[32] I. Y. Aref'eva, A. Hajilou, P. Slepov, and M. Usova, Phys. Rev. D **111**, 046013 (2025).
[33] W.-B. Chang and D. F. Hou, Phys. Rev. D **109**, 086010 (2024).
[34] M. Hippert, J. Grefa, T. A. Manning, J. Noronha, J. Noronha-Hostler, I. P. Vazquez, C. Ratti, R. Rougemont, and M. Trujillo, Phys. Rev. D **110**, 094006 (2024).
[35] X. Chen, D. Li, and M. Huang, Chin. Phys. C **43**, 023105 (2019).
[36] X. Chen, D. Li, D. Hou, and M. Huang, J. High Energy Phys. 03 (2020) 073.
[37] J. Zhou, X. Chen, Y.-Q. Zhao, and J. Ping, Phys. Rev. D **102**, 086020 (2020).
[38] X. Chen, L. Zhang, and D. Hou, Chin. Phys. C **46**, 073101 (2022).
[39] X. Chen and M. Huang, Phys. Rev. D **109**, L051902 (2024).
[40] B. Chen, X. Chen, X. Li, Z.-R. Zhu, and K. Zhou, Phys. Rev. D **111**, 086033 (2025).
[41] X. Chen and M. Huang, J. High Energy Phys. 02 (2025) 123.
[42] Y. Chen, X. Chen, D. Li, and M. Huang, Phys. Rev. D **111**, 046006 (2025).
[43] S. Lin, X. Liu, X. Chen, G.-F. Zhang, and J. Zhou, Phys. Rev. D **111**, 046005 (2025).
[44] N. Jokela, M. Järvinen, and A. Piispa, Phys. Rev. D **110**, 126013 (2024).
[45] L. Zhu, X. Chen, K. Zhou, H. Zhang, and M. Huang, Phys. Rev. D **112**, 026019 (2025).
[46] B. Chen, X. Chen, M. Fujita, and J. Zhang, J. High Energy Phys. 09 (2025) 046.
[47] F. Sun, X. Chen, S. Li, and A. Watanabe, arXiv:2503.17642.
[48] L. Zhang, L. Yin, G.-D. Zhou, C.-J. Fan, and X. Chen, Phys. Rev. D **111**, 126001 (2025).
[49] X. Chen, Y. Chen, and K. Zhou, Phys. Rev. D **112**, 126025 (2025).
[50] L. Zhu, O.-Y. Luo, X. Chen, K. Zhou, H. Zhang, and D. Hou, Nucl. Sci. Tech. **37**, 68 (2026).
[51] B. Chen, L. Zhu, X. Chen, D. Hou, and X. Chen, arXiv:2508.16167.
[52] J.-Y. Shen, X.-Y. Liu, J.-R. Wu, Y.-L. Wu, and Z. Fang, arXiv:2511.19127.
[53] H.-S. Jeong, H. Kim, K.-Y. Kim, G. Yun, H. Yu, and K. Yun, arXiv:2511.22522.
[54] L. Zhang and M. Huang, Phys. Rev. D **106**, 096028 (2022).
[55] U. Gursoy, M. Jarvinen, and G. Nijs, Phys. Rev. Lett. **120**, 242002 (2018).
[56] H. Bohra, D. Dudal, A. Hajilou, and S. Mahapatra, Phys. Lett. B **801**, 135184 (2020).
[57] I. Y. Aref'eva, A. Hajilou, K. Rannu, and P. Slepov, Eur. Phys. J. C **83**, 1143 (2023).
[58] H.-A. Zeng, L. Wang, and M. Huang, arXiv:2512.06044.
[59] A. Bazavov *et al.* (HotQCD Collaboration), Phys. Rev. D **90**, 094503 (2014).
[60] A. Bazavov *et al.* (HotQCD Collaboration), Phys. Rev. D **86**, 034509 (2012).
[61] A. Bazavov *et al.*, Phys. Rev. D **95**, 054504 (2017).
[62] S. Borsanyi, G. Endrodi, Z. Fodor, A. Jakovac, S. D. Katz, S. Krieg, C. Ratti, and K. K. Szabo, J. High Energy Phys. 11 (2010) 077.
[63] D. Bollweg, J. Goswami, O. Kaczmarek, F. Karsch, S. Mukherjee, P. Petreczky, C. Schmidt, and P. Scior (HotQCD Collaboration), Phys. Rev. D **105**, 074511 (2022).
[64] P. Colangelo, F. Giannuzzi, S. Nicotri, and F. Zuo, Phys. Rev. D **88**, 115011 (2013).
[65] C. Ecker, N. Jokela, and M. Järvinen, Phys. Rev. D **113**, L041302 (2026).
[66] S. Borsanyi, Z. Fodor, J. N. Guenther, P. Parotto, A. Pasztor, C. Ratti, V. Vovchenko, and C. H. Wong, Phys. Rev. D **112**, L111505 (2025).
[67] D. A. Clarke, P. Dimopoulos, F. Di Renzo, J. Goswami, C. Schmidt, S. Singh, and K. Zambello, Phys. Rev. D **112**, L091504 (2025).